JOURNAL OF GUIDANCE, CONTROL, AND DYNAMICS
Vol. 25, No. 4, July–August 2002

Fast Prediction Algorithms of Satellite Imaging Opportunities with Attitude Controls

Shu-Fan Wu* and Phil L. Palmer†
University of Surrey, Guildford, England GU2 7XH, United Kingdom

The imaging prediction problems for satellite Earth observing missions are discussed. The imaging opportunities are first distinguished from the nadir tracking points with maximum elevation angles. A fast prediction approach is then presented, consisting of three steps: the coarse search, the imaging estimation, and the imaging refinement. Innovative algorithms are developed to complete the appropriate estimation and refinement tasks for different working modes, considering both a canted camera and available attitude maneuvers. The algorithms are evaluated through computational experiments and further tested with applications in practical satellite mission management. Further applications include in-orbit real-time autonomous mission management and operations onboard satellites.

I. Introduction

WITH the requirements toward the "smaller, faster, cheaper" strategy in space missions, low-cost, fast access, and multifunctional small satellites are being increasingly used to provide and exchange information for a wide variety of professions, such as Earth observing, monitoring, surveying, mapping, as well as communications. To reach a larger swath coverage and provide sufficient revisit times for certain mission requirements, constellations of a certain number of satellites are required. One example is the Disaster Monitoring Constellation,[1] which is made up by five low-cost enhanced microsatellites, aiming at the first low-cost and integrated Earth-observation constellation in the world dedicated to the humanitarian objectives of disaster assessment and monitoring. A more commercial satellite network is the "GANDER" mission,[2] which will comprise a constellation of 16 microsatellites, aiming at providing commercial services on predictions and forecasts of maritime conditions through measuring the significant sea wave height and sea surface wind velocity. For these kinds of complicated space missions, greater operability and onboard autonomy of satellites become crucial to reduce the cost for both ground and onboard operations. Thus fast and smart algorithms are required for some traditional technical problems for the purpose of onboard real-time implementation and autonomous operation.

One important technical problem in imaging missions is how to determine or predict the time moment when the camera onboard the satellite is in the optimal position for imaging a target on the Earth's surface. As the satellite may not fly directly over the desired target area for some periods (days or weeks), in-orbit attitude maneuvers are required to point the camera onto the target to get more opportunities for imaging. Then the required attitude angles of the satellite for imaging the targets need also to be determined or predicted in advance. Furthermore, the camera is sometimes mounted with a canted angle off the stabilized nadir axis, such as in the case of the microsatellite Tsinghua-1, where the camera was mounted at a canted angle of −19 deg around its flight direction. This makes the prediction process even more sophisticated.

The imaging prediction problem is closely related to the satellite pass prediction[3] or the so-called rise-and-set time problem of when a satellite is visible from a given point, e.g., ground station, on the Earth. However, the imaging problem is made more complicated by involving camera information and potential satellite attitude maneuvers. As a classical problem, the rise-and-set time computation has been discussed in quite a few publications.[3–8] The traditional approach, so-called trajectory checking, is to let the satellite run through its ephemeris and to check at each instant where the subsatellite nadir point falls and whether it becomes visible to a specified ground location. This method requires Keplerian equations to be solved hundreds of times per orbit period[4] and is therefore fairly computationally expensive. Escobal[4] proposed a faster method to solve this problem by developing a closed-form solution for the visibility periods. A single transcendental equation, called the *controlling equation*, was introduced as a function of the eccentric anomaly of the satellite orbit. Numerical methods were then used to find the rise- and -set times. This method offers the advantage that the controlling equation is solved only once per orbital period. However, it is only valid for two-body motions, which produce large errors for long-term prediction. Lawton[5] has developed another method to solve for satellite-satellite and satellite-ground station visibility periods for vehicles in circular or near circular orbits by approximating the visibility function. Alfano[6] and Vallado[8] further developed the visibility function to suit all orbital types. However, these methods are only valid for solving satellite rise-and-set time problems for short-term periods.

Recently, a new method and fast algorithm for both the long-term LEO satellite pass prediction (or the rise-and-set time prediction) and the maximum elevation angle time prediction (or nadir tracking problem) over a specified ground target has been developed.[3,7] Based on an analytic description of the orbit,[9] the new algorithm takes into account both the secular perturbations and the short and long periodic perturbations from the geopotential in a simple form. Furthermore, it includes a straightforward atmospheric drag model derived from the well-acknowledged NASA atmospheric statistics, which is represented by a variable parameter subject to modification according to periodic atmospheric changes. The proposed formulation needs to be solved only twice per day, which makes the new algorithm much faster (by several orders of magnitude[3,7]) than the exhaustive search using an SGP4[10] propagation model, while keeping a high accuracy over a long period.

In imaging missions the maximum elevation time is often treated as the imaging time in many low-Earth-orbit (LEO) microsatellite applications.[7] In reality, however, the best imaging point is slightly shifted from the maximum elevation point caused by the Earth's oblateness and orbital eccentricity. The magnitude of this shift is mainly a function of target latitude and orbital eccentricity. As will be illustrated by the computation results in this paper, for the microsatellite Tsinghua-1 and the ground target of Guildford, United Kingdom, the time shifts will be around 0.28 s for nadir pointing and around 1.5 s for a canted camera with-20 deg, corresponding a distance shift of around 1.6 and 12 km in the target-centered local

Received 17 December 2000; revision received 14 June 2001; accepted for publication 31 July 2001; presented as Paper 2001-4270 at the AIAA Guidance, Navigation, and Control Conference, Montreal, QC, Canada, 6–9 August 2001.

*Research Fellow, Surrey Space Center; Shufan.Wu@surrey.ac.uk.
†Reader, Surrey Space Center; P.Palmer@surrey.ac.uk.

horizontal (LH) plane. These errors are not acceptable for high-resolution imaging.

Although there have been a number of publications discussing the traditional rise-and-set time and the nadir tracking problems, the algorithms of predicting the best imaging opportunities when counting a canted camera and available satellite attitude maneuvers have not yet been reported. This paper will present the innovative algorithms to handle these problems and present some test results from the Tsinghua-1 satellite. To cover a wider range of imaging missions for different cases, four working modes have been investigated: 1) imaging opportunities with a canted camera and nadir pointing (no attitude maneuvers), 2) imaging opportunities with a canted camera and yawing maneuvers, 3) imaging opportunities with a canted camera and rolling maneuvers, and 4) image projection onto the Earth's surface at a given time and specified satellite attitudes.

This paper is organized as follows. Section II describes the prediction principle and the basic algorithms for the first working mode. Sections III–V discuss the specific algorithms for the other three working modes. Section VI presents some test computation results. Section VII summarizes the major achievements of this paper.

II. Prediction Principle and Algorithms for the First Working Mode

A. Conditions of the Imaging Point

The best imaging opportunity of a satellite camera is defined as two cases in this paper. The first is the time when the camera's boresight (the focus center line) is exactly pointing at the specified target with appropriate attitude control of the satellite. The second case is the time point when the target is within the camera's field of view (FOV) and the distance between the target and the camera's optical axis projected onto the LH plane is minimized with respect to the flight time. For the first case it is assumed that attitude controls of the satellite are available. The second case occurs when no attitude maneuvers are available or when the target is out of the allowed attitude maneuvering ranges as a result of certain considerations, such as image distortion, etc.

For the first case the imaging condition is simply when the onboard camera's boresight coincides with the target slant, which is defined as the vector connecting the satellite and the ground target. For the second case the condition becomes slightly complicated. As a satellite flies along its orbit, the projected point of the camera's boresight onto the LH plane would form a track that is locally a straight line (for long distances it might have some very small curvatures), as shown in Fig. 1. The shadow point of the camera would move along this line with a two-dimensional velocity $\boldsymbol{V}_L$, then at the best point of imaging the position vector $\boldsymbol{r}_L$ of the shadow point should be perpendicular to its velocity vector. Thus the conditional equation for the optimal imaging opportunities at this case is

$$\boldsymbol{r}_L \cdot \boldsymbol{V}_L = 0 \tag{1}$$

B. Prediction Principle

The task of imaging prediction algorithms is to find the potential points where the preceding imaging conditions are met. The prediction scheme developed in this paper is to divide this complicated task into three successive steps. First, a coarse search process is applied to find out the potential satellite passes that offer possible imaging opportunities. Then, an imaging estimation process is adopted to estimate the appropriate imaging time based on the coarse search results and the spherical geometry, as well as the target and satellite orbital information. In the preceding two steps the Earth is regarded as an ideal sphere, and the satellite's orbit is treated as a circle, which would bring errors in the estimation results. Computation results showed the errors are normally within a few seconds (1–3 s) for LEO satellites used in this research.

An imaging refinement process is finally taken to compensate the errors in the estimation results. Accurate satellite orbital solution and practical Earth shape model, together with the target parameters, are used to solve the conditional equations of the imaging point. For each working mode appropriate iteration algorithms are developed to refine the time prediction.

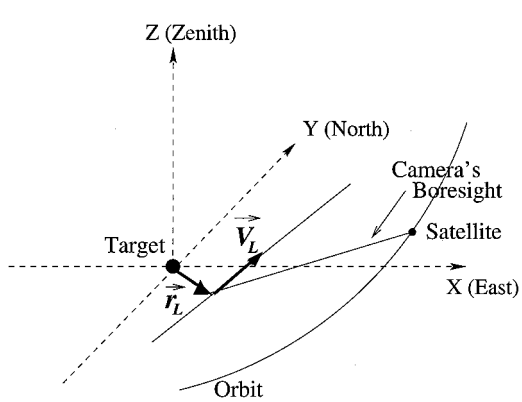

Fig. 1 Imaging condition in LH plane.

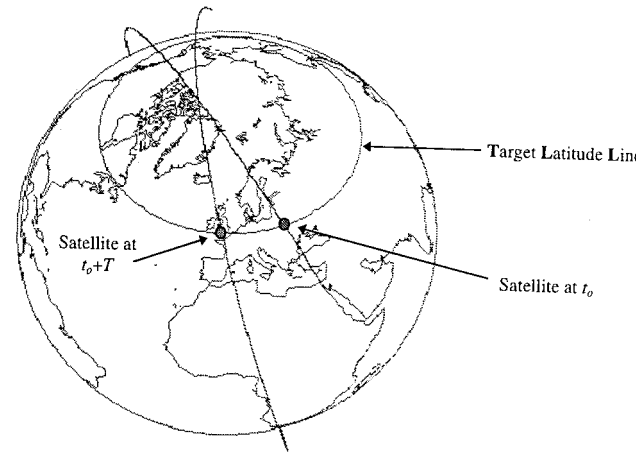

Fig. 2 Movement of satellite footprint along TLL when orbiting around the Earth.

C. Coarse Search for Interested Satellite Passes

The basic principle of the coarse search algorithm is the fact that for two-body motion a satellite will revisit exactly the same point in an inertial coordinate system after each orbital period T,[3,7] as illustrated in Fig. 2. While the Earth rotates along its eigenaxis, the target will move along the target latitude line (TLL), which is defined as the small circle of constant latitude that runs through the target location. Thus, in the inertial space after each orbital period that the satellite revisits the TLL the Earth's rotation will bring the target closer to the satellite's longitudinal position along the TLL. In other words, the satellite will see the target approaching by an amount $\omega_\oplus T$ or $\omega_\oplus 2\pi/n$, where $\omega_\oplus$ is the Earth's rotation rate, n is the orbital mean motion, and T is the orbital period. In the Earth-centered Earth-fixed (ECEF) coordinates, the target will see the satellite's longitude at TLL crossing approach or leave from the target longitude with a step of $\omega_\oplus T$ after each orbit. This relation could be described by the following equation:

$$\Delta\upsilon = \upsilon_S - \upsilon_T = N\omega_\oplus 2\pi/n + \mathrm{d}\upsilon \tag{2}$$

where $\Delta\upsilon$ is the initial longitude difference between the satellite footprint (υ_S) when first crossing the TLL at time t_0 and the specific target on the ground (υ_T); N is the number of satellite revolutions since t_0; $\mathrm{d}\upsilon$ is the longitudinal difference angle between satellite footprint and target at time $t = t_0 + NT$.

This equation builds up a very simple and fast relation between the target and satellite footprint longitudes as a function of time, which forms the core part of the fast coarse search algorithms for satellite passes. To account for secular perturbations and drag effects, some modifications were introduced to the preceding equation; details can be found in Refs. 3 and 7.

On the other hand, the finite FOV of the camera will cover a certain belt on the Earth's surface as a satellite flies along its orbit, as illustrated in Fig. 3a, where τ represents the canted angle of the camera with reference to the nadir direction and γ is the camera's

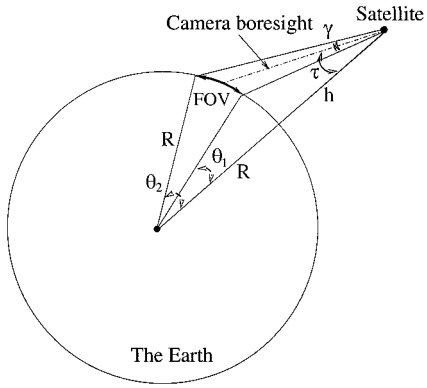

a) Sphere angle of imaging belt

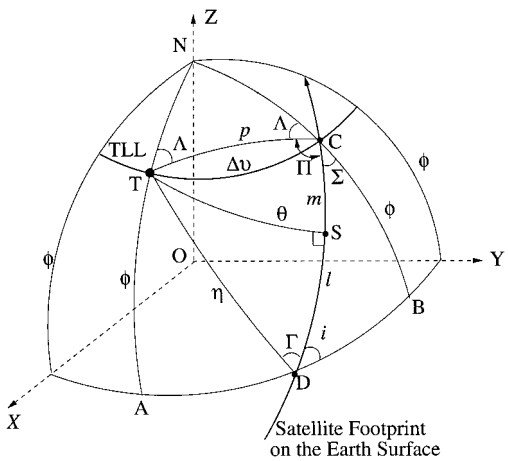

b) Spherical geometry

Fig. 3 Coarse search and imaging estimation geometries.

FOV. The border of the imaging swath can be represented by the angles θ_1 and θ_2, which are calculated by the following equations:

$$\theta_1 = \sin^{-1}\{[(R+h)/R]\sin(\tau - \gamma/2)\} - (\tau - \gamma/2) \tag{3}$$

$$\theta_2 = \sin^{-1}\{[(R+h)/R]\sin(\tau + \gamma/2)\} - (\tau + \gamma/2) \tag{4}$$

where R is the Earth's radius and h is the satellite altitude. As both R and r change as the satellite moves along its orbit, these two angles are not constants in time. However, for LEO Earth observation satellites their orbits are normally near circular and polar. For simplicity, the orbital semimajor axis and the Earth's equatorial radius are used in the preceding equations to get constant offset angles. That is, the Earth is assumed to be an ideal sphere and the satellite's orbits are assumed to be an ideal circle. These assumptions introduce errors in the coarse search results, which will be nulled out in the final imaging refinement process.

To connect the imaging border angles with the satellite longitude position along TLL, the border angle is further transferred as a longitude offset angle along the TLL, with a spherical Earth, as shown in Fig. 3b. The following equations are used to transfer angle θ_1 and θ_2 into longitude offset angles $\Delta\upsilon_1$ and $\Delta\upsilon_2$ (Refs. 7 and 9):

$$\Delta\upsilon = \cos^{-1}\left(\frac{\cos p - \sin^2\phi}{\cos^2\phi}\right) \tag{5}$$

$$\cos p = \cos l \cos\eta + \sin l \sin\eta \cos\Gamma \tag{6}$$

$$\tan\Gamma = \frac{\sin\theta \sin i}{\sin\phi - \cos i \sin\theta} \tag{7}$$

$$\sin\eta = \frac{\sin\theta}{\sin\Gamma} \tag{8}$$

$$\sin l = \frac{\sin\phi}{\sin i} \tag{9}$$

where ϕ is the target latitude; i is the satellite orbit inclination angle; ρ, η, and l are spherical angles (arc lengths) along corresponding great circles; and Γ is a rotation angle, as illustrated in Fig. 3b. The preceding formulas have been derived for the case of $\theta > 0$ and $\phi \geq 0$. For the case of $\theta < 0$, Eq. (5) should be modified as

$$\Delta\upsilon = \text{sign}(\theta) \cdot \cos^{-1}\left(\frac{\cos p - \sin^2\phi}{\cos^2\phi}\right) \tag{5a}$$

For the case of $\phi < 0$, Eqs. (7) and (9) should to be modified as follows, whereas Eqs. (6) and (8) remain the same:

$$\tan\Gamma = -\frac{\sin\theta \sin i}{\sin\phi - \cos i \sin\theta} \qquad (\phi < 0) \tag{7a}$$

$$\sin l = -\frac{\sin\phi}{\sin i} \qquad (\phi < 0) \tag{9a}$$

Back to the relative motion between the target and satellite footprint on TLL, when the relative difference between the longitudes of the target and satellite footprint on TLL meet the relation

$$\Delta\upsilon_2 \geq \mathrm{d}\upsilon \geq \Delta\upsilon_1 \tag{10}$$

then the target will be within the camera's FOV in width, which means a potential imaging opportunity arises. Thus the approximate time (or phase angle) of the satellite as it passes through the TLL within a relevant longitude range can be determined rapidly, without involving the satellite's orbital propagation equations.

Because of the assumptions that the Earth is an ideal sphere and the orbit is circular, there are potentials for the coarse search algorithms to eliminate some pass opportunities that would give imaging chances. Analyses revealed that it happens only on those potential imaging chances where the target is located around the border of the camera's FOV. On the other side, there are also potential passes that satisfy the coarse search process while the target is actually outside the camera's FOV when using accurate Earth model and orbital information. To compensate for these shortcomings, a small margin (0.5–1 deg) is added to the FOV angle in computing the imaging swath by Eqs. (3) and (4). Then in the final results the miss distance between the target and the camera's boresight projection point in the LH plane is calculated. Those imaging chances whose miss distances are out of the camera's actual FOV range should be discarded.

D. Imaging Estimation Algorithms

After the coarse search process the relevant satellite passes are determined in the form of the times of TLL passage. The next step is to determine the imaging position subject to different imaging modes. For the first mode, without attitude control, the imaging point should be located near the point S in Fig. 3b, where the great circle connecting S with the target should be perpendicular to the orbital plane CD. Again the Earth is assumed to be an ideal sphere so that we can compute the arc length (spherical angle) CS from spherical trigonometry.[9] The longitude offset angle $\Delta\upsilon$ is equal to $\mathrm{d}\upsilon$ in Eq. (2). First, from Eq. (5) arc TC could be determined:

$$\cos p = \sin^2\phi + \cos^2\phi \cdot \cos\Delta\upsilon \tag{11}$$

From the right spherical triangle BCD the rotation angle Σ (between CD and CB) is

$$\cos\Sigma = \frac{\cos l \cdot \sin i}{\cos\phi} \tag{12}$$

Then from spherical triangle NTC, the rotational angle Λ is

$$\sin\frac{\Lambda}{2} = \sqrt{\frac{\cos(\phi + p/2)}{2\cos(p/2) \cdot \cos\phi}} \tag{13}$$

Finally, with the spherical triangle CTS the rotation angle Π and the length m of the arc CS can be determined as

$$\Pi = \pi - \Lambda - \Sigma \tag{14}$$

Table 1 Computation algorithms of the phase angle offset *m*

Inclination angle i	Satellite phase angle α at TTL	Longitude offset $\Delta\upsilon \geq 0$	Longitude offset $\Delta\upsilon < 0$
$0 < i < \pi/2$	$0 \leq \alpha < \pi/2$	$\tan^{-1}[\cos(\Lambda + \Sigma) \cdot \tan p]$	$\tan^{-1}[\cos(\Lambda - \Sigma) \cdot \tan p]$
	$\pi \leq \alpha < 3\pi/2$	$(m < 0)$	$(m > 0)$
	$\pi/2 \leq \alpha < \pi$	$-\tan^{-1}[\cos(\Lambda - \Sigma) \cdot \tan p]$	$-\tan^{-1}[\cos(\Lambda + \Sigma) \cdot \tan p]$
	$3\pi/2 \leq \alpha < 2\pi$	$(m < 0)$	$(m > 0)$
$\pi/2 < i < \pi$	$0 \leq \alpha < \pi/2$	$\tan^{-1}[\cos(\Lambda - \Sigma) \cdot \tan p]$	$\tan^{-1}[\cos(\Lambda + \Sigma) \cdot \tan p]$
	$\pi \leq \alpha < 3\pi/2$	$(m > 0)$	$(m < 0)$
	$\pi/2 \leq \alpha < \pi$	$-\tan^{-1}[\cos(\Lambda + \Sigma) \cdot \tan p]$	$-\tan^{-1}[\cos(\Lambda - \Sigma) \cdot \tan p]$
	$3\pi/2 \leq \alpha < 2\pi$	$(m > 0)$	$(m < 0)$

$$m = \tan^{-1}[\cos(\Lambda + \Sigma) \cdot \tan p] \tag{15}$$

The estimated imaging point S is then determined as

$$\alpha_S = \alpha_C + m \tag{16}$$

where α_S and α_C represent the epicycle phase angle of the satellite at the points S and C. The preceding algorithms are developed for the case of $0 \leq \alpha_S < \pi/2$, $\Delta\upsilon \geq 0$, and $i < 90$ deg, as illustrated in Fig. 3b. When the satellite falls within other phase angle ranges, when $\Delta\upsilon < 0$, and when $i > 90$ deg, the geometrical relations of the target and satellite are different. Analyses show that Eqs. (11–13) and (16) remain the same, whereas Eq. (14) and therefore Eq. (15) change slightly. Table 1 lists the algorithms of computing m for all possible cases.

For the second mode with attitude control over yaw, the perpendicular point S is not the approximate imaging point. Then new algorithms are required to estimate the imaging points when counting for the attitude maneuvers, as will be discussed in Sec. III.

E. Imaging Refinement Algorithms

The refinement process will use the accurate Earth and orbital information to determine the best imaging points according to the conditions discussed in Sec. II.A. As the conditional equations cannot be solved directly through closed algebraic relations, iteration algorithms are developed to get the required accuracy.

To refine the estimation results, accurate satellite orbit propagation is required to get the exact satellite position and velocity information at the time of interest. The following epicycle equations,[11,12] which use four redundant coordinates to describe the satellite's orbital propagation, are used in the refinement algorithms:

$$r = a(1 + \rho) - A\cos(\alpha - \alpha_p) + a\chi \sin\beta + a\Delta_r \cos 2\beta - 2B\beta \tag{17}$$

$$i = i_0 + \Delta_I(1 - \cos 2\alpha) \tag{18}$$

$$\Omega = \Omega_0 + \theta\alpha + \Delta_\Omega \sin 2\alpha \tag{19}$$

$$\lambda = \beta + 2A/a[\sin(\alpha - \alpha_p) + \sin\alpha_p] - 2\chi(1 - \cos\beta) + \Delta_\lambda \sin 2\beta + \tfrac{3}{2}B\beta^2 \tag{20}$$

$$\beta = (1 + \kappa)\alpha = (1 + \kappa)nt \tag{21}$$

where r is the satellite radius to the Earth's centre; i the inclination; Ω the right ascension of the ascending node; λ the argument of latitude; ρ, κ, and θ are coefficients for secular perturbation; χ is the long periodic perturbation coefficient; Δ_x represent the short periodic terms; and B is the epicycle drag coefficient. For a LEO satellite with its orbit eccentricity being not larger than 0.005, the preceding epicycle equations give a direct solution of the satellite position with reference to time, with a better accuracy than the results by using the SGP4 propagation approach.[10,11]

The satellite's coordinates are given as a function of time from the preceding equations in the local orbit (LO) coordinate frame and are then transformed into the Earth-centered inertial (ECI), ECEF, and local tangent (LT) coordinates successively. LT represents the local tangent coordinate, where the center is defined at the target located on the Earth's surface, the x axis points to the east direction, the y axis points to the north direction, and the z axis completes the right-handed systems. Its x–y plane is the so-called LH plane. Meantime, the unit orientation vector of the camera's boresight is calculated in the satellite body axes, according to the given information (canted angle, etc.), and is then transformed into the LO, ECI, ECEF, and LT axes successively. Thus the slant vector from the target to the satellite is obtained as the satellite position vector in LT axes. From the orientation vector of the camera's boresight, the position vector $\boldsymbol{r}_L$ of the camera's boresight shadow on the LH plane can be easily determined, as depicted in Fig. 1.

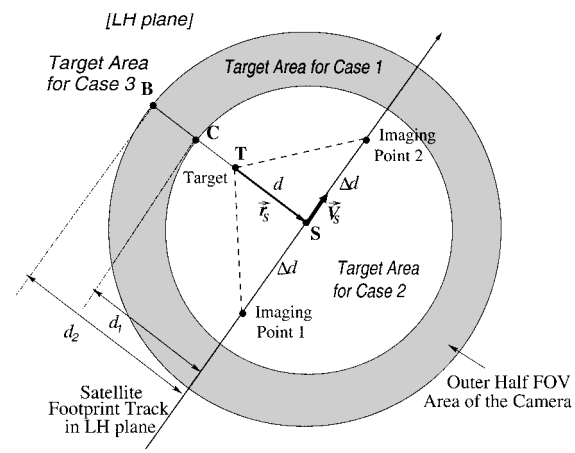

Fig. 4 Imaging geometry with yawing maneuvers in LH plane.

The velocity vector $\boldsymbol{V}_L$ of the shadow point P on the LH plane is also required to evaluate the imaging condition of Eq. (1). It can be calculated by differentiating the epicycle equations and performing similar frame transformations. We have adopted a simpler approach to compute two successive shadow points on LH plane with a small time difference and subtract them to get an average velocity vector, which could be considered as the local velocity when the time step is set small enough.

The time error of the current satellite position to the required position, which meets exactly the imaging condition Eq. (1), can be calculated as

$$\Delta t = -\boldsymbol{r}_L \cdot \boldsymbol{V}_L \big/ V_L^2 \tag{22}$$

This time error is added to the estimated time to get a new evolved satellite point and its camera's boresight shadow point in the LH plane. An iteration process is applied based on this algorithm to reduce the time error to be within an allowed tolerance.

III. Prediction Algorithms with Yaw Attitude Maneuvers

With full yaw maneuvering capabilities the covering area of possible imaging with a canted camera could be increased greatly, becoming a big circle belt around the satellite footprint on the Earth's surface, as depicted in Fig. 4. There might be one or two imaging opportunities during a potential pass, which makes the prediction much more complicated than the first working mode. Correspondingly, the prediction algorithms for all three of the steps need to be modified or extended.

For coarse search the spherical angle offsets defining the width of the imaging area on the Earth's surface should be calculated from the following equations, instead of Eq. (3) and (4), whereas the search algorithm remains the same as in Sec. II:

$$\theta_1 = -\sin^{-1}\{[(R+h)/R]\sin(|\tau| + \gamma/2)\} - (|\tau| + \gamma/2) \quad (23)$$

$$\theta_2 = \sin^{-1}\{[(R+h)/R]\sin(|\tau| + \gamma/2)\} - (|\tau| + \gamma/2) \quad (24)$$

For imaging estimation the algorithms discussed in Sec. II are first used to determine the approximate point where the great circle connecting the satellite footprint and the target is perpendicular to the orbital plane. Then the following three steps are further applied to determine and estimate the approximate imagining points:

1) Pointing the camera to the target side is the first point. As the yaw maneuver provides a full rotation of the canted camera around the nadir axis, the initial camera's position could point either to the target side or to the opposite side with reference to the satellite ground track. An algorithm is then required to check the relative relations and define an initial yaw angle (0 or π) to point the camera to the target side. First, the position vector $\boldsymbol{r}_S = (r_x, r_y)$ and velocity vector $\boldsymbol{V}_S = (V_x, V_y)$ of the satellite nadir footprint in the LH plane are calculated with the method discussed in Sec. II.E. Then its cross product is computed as follows:

$$z = |\boldsymbol{r}_S \times \boldsymbol{V}_S| = r_x V_y - r_y V_x \quad (25)$$

With the sign of z and the canted angle, an initial yaw angle Ψ_0 can be determined according to Table 2.

2) Determining how many imaging opportunities exist for this pass is the second point. For a potential imaging pass with available yaw maneuver, there are three cases for imaging estimation, with 0, 1, or 2 imaging points, respectively, as illustrated in Fig. 4. To determine which case is relevant for a specific pass, the camera's boresight and its outside FOV limit direction (with a canted angle of $\tau + \gamma/2$) are projected onto the LH plane to get two more points, C and B, in Fig. 4. Then the distances to the satellite footprint S from the target T, camera's boresight point C, and outer border limit point B are calculated as d, d_1, and d_2, respectively, as illustrated in Fig. 4, for the case when target is located within the camera's boresight range. In this case there are two potential imaging points during the pass. The three distance values determine how many potential imaging opportunities there will be in this pass, as listed in Table 3.

3) Estimating the approximate imaging points is the final point. For case 1 the target location is within the outer half FOV of the camera. The camera's boresight cannot point exactly at the target, which means a miss distance exists. In this case no more yawing maneuver is required. The estimated point S becomes the imaging point submitted for further refinement.

For case 2 the target location is within the camera's boresight maneuvering ranges. Thus two imaging chances exist, and further yaw maneuvers are required to point the camera's boresight exactly on the target. As an approximate estimation, the camera's boresight track on the LH plane with a 2π yawing maneuver is assumed to be a circle centered at the satellite footprint along its track line, as shown in Fig. 4. Then the approximate distance and traveling time of the two imaging chances to the current satellite position within the LH plane are calculated approximately by the following equation:

$$\Delta d = \sqrt{d_1^2 - d^2} \quad (26)$$

$$\Delta t = \Delta d / V_S \quad (27)$$

where V_S is the magnitude of the velocity of the satellite's footprint on the LH plane, as in Eq. (25). The imaging estimation is achieved by adding/subtracting the time offset of Eq. (27) to/from the flight time of point S. For case 3 the pass is regarded as being not able to image the target.

Finally, the imaging refinement algorithm is applied to get the accurate imaging time. The refining process is different for the first two cases of imaging opportunities listed in Table 3. For case 1 the imaging condition is still Eq. (1), hence the refining process and algorithms are the same as discussed in Sec. II.E. The position and velocity vectors of the camera's boresight shadow on the LH plane are used for the iteration process in time, with the algorithms based on Eq. (22). The required yaw angle is just the initial yawing angles from Table 2.

In case 2 the situation becomes much more complicated. The imaging condition requires that the camera's boresight points at the target exactly. As the cant angle is fixed in this working mode, the angle between the satellite nadir direction and the slant vector from the satellite to the target should be equal to the camera's canted angle, which can be described by the following equation:

$$-\boldsymbol{r} \cdot \boldsymbol{s} = |\boldsymbol{r}| \cdot |\boldsymbol{s}| \cdot \cos\tau \quad (28)$$

where $\boldsymbol{r}$ represents the satellite's position vector in ECEF and $\boldsymbol{s}$ represents the slant vector in ECEF from the satellite to the target. This equation is the new imaging condition, instead of Eq. (1). As both $\boldsymbol{r}$ and $\boldsymbol{s}$ are functions of the flight time, Eq. (28) is a nonlinear function of the flight time around the estimated point. Analytic solutions are not available, or very complicated if not impossible, for this equation, thus a numerical iteration algorithm is used here.

From Fig. 5 the angle ξ between $\boldsymbol{r}$ and $\boldsymbol{s}$ is first computed, and the difference angle ϵ between $\boldsymbol{s}$ and the camera's boresight direction (line SC in Fig. 5a) is obtained from

$$\epsilon = \xi - |\tau| = \cos^{-1}\left(\frac{\boldsymbol{r} \cdot \boldsymbol{s}}{|\boldsymbol{r}| \cdot |\boldsymbol{s}|}\right) - |\tau| \quad (29)$$

Then, the distances from the camera's boresight point to the target (e_1) and to the satellite footprint (e_2) in the LH plane can be calculated as

$$e_1 = |\boldsymbol{s}| \sin\epsilon / \sin(\epsilon + \sigma) \quad (30)$$

$$e_2 = |\boldsymbol{s}| \sin\xi / \sin(\xi + \sigma) - e_1 \quad (31)$$

where σ is the elevation angle of the slant vector from the target to the satellite, which can be computed by transforming $\boldsymbol{s}$ from ECEF into LT and computing its elevation angle with reference to the LH plane. The miss distance e_1, however, is not the distance error along the satellite track direction. As shown in Fig. 5b, there is a cross angle ν between the miss distance direction and the flight velocity direction, and this angle is not close to 90 deg in the working mode

Table 2 Initial yaw angle to point the camera toward target

Ψ_0	$\tau > 0$	$\tau < 0$
$z > 0$	0	π
$z < 0$	π	0

Table 3 Initial yaw angle to point the camera toward target side

Parameter	Case 1	Case 2	Case 3
Conditions	$d_2 \geq d \geq d_1$	$d < d_1$	$d > d_2$
Imaging chances	1	2	0

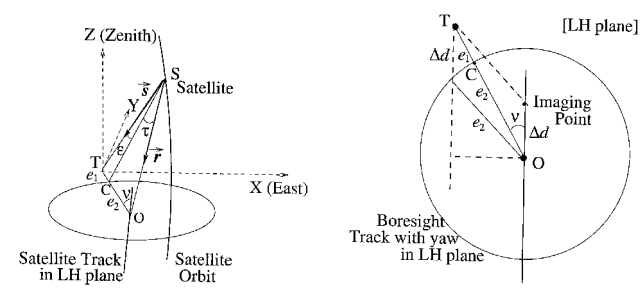

a) In TLT axes b) In LH plane

Fig. 5 Geometrical relation for imaging with yaw maneuver.

with yaw maneuvers. From the geometrical relation within the LH plane, the component of the miss distance in parallel with the satellite moving direction can be computed as

$$\Delta d = (e_1 + e_2)\cos\nu - \sqrt{e_2^2 - (e_1 + e_2)^2 \sin^2\nu} \tag{32a}$$

Thus the time iteration amount is obtained as

$$\Delta t = \Delta d / |\boldsymbol{V}_S| \tag{33}$$

The preceding algorithm is used for the refining iteration process until the time error falls within the specified tolerance. Computation tests demonstrated that the preceding refining algorithms converge very quickly, with two or three iterations to achieve an accuracy of within 0.02 s. For the case of negative ϵ and e_1, the preceding algorithms remain the same, whereas for the case of $\nu > \pi/2$, Eq. (32) needs to be modified:

$$\Delta d = (e_1 + e_2)\cos\nu + \sqrt{e_2^2 - (e_1 + e_2)^2 \sin^2\nu} \tag{32b}$$

With the iteration results the slant vector $\boldsymbol{s}$ converges to the camera's boresight. The final yawing attitude required for image capture is then the azimuth angle of the slant vector in the LO axes. Thus by transforming the slant vector $\boldsymbol{s}$ from ECEF into ECI and LO, the second yaw angle offset is then computed. The final yaw control requirement is the combination of this angle with the initial yaw angle placement listed in Table 2.

IV. Prediction Algorithms with Roll Attitude Maneuvers

With a roll maneuver the camera could cover a much wider imaging belt on the Earth's surface. However, because of considerations of imaging distortion the roll angle of the camera's boresight from the nadir direction should be limited. Defining this maximum roll angle as $\Phi_{\max}$, if the target is required to be centered in the image then the spherical angle offsets defining the imaging width [Eqs. (3) and (4) in Sec. II] should be replaced by the following equations:

$$\theta_1 = -\sin^{-1}\{[(R + h)/R]\sin\Phi_{\max}\} - \Phi_{\max} \tag{34a}$$

$$\theta_2 = \sin^{-1}\{[(R + h)/R]\sin\Phi_{\max}\} - \Phi_{\max} \tag{35a}$$

If the target is only required to be within the FOV of the camera, i.e., located within the borders of the image, then the angle offset will be slightly bigger by taking into account the FOV angle:

$$\theta_1 = -\sin^{-1}\{[(R + h)/R]\sin(\Phi_{\max} + \gamma/2)\} - (\Phi_{\max} + \gamma/2) \tag{34b}$$

$$\theta_2 = \sin^{-1}\{[(R + h)/R]\sin(\Phi_{\max} + \gamma/2)\} - (\Phi_{\max} + \gamma/2) \tag{35b}$$

In this mode there is only one imaging opportunity during each pass. Thus imaging estimation algorithms are the same as discussed in Sec. II.

For imaging refinement the following process is applied. First, the refinement algorithms discussed in Sec. II.E are used to find the point where the position and velocity vectors of the satellite shadow point on the LH plane is perpendicular to each other. Then, the angle between the slant vector pointing to the target and satellite nadir pointing direction is computed as the approximate magnitude of the net roll angle of the camera's boresight, and Eq. (25) is further used to determine the sign of the required roll angle. That is,

$$\Phi_B = \text{sign}(z) \cdot \cos^{-1}\left(\frac{\boldsymbol{r}\cdot\boldsymbol{s}}{|\boldsymbol{r}|\cdot|\boldsymbol{s}|}\right) \tag{36}$$

where z is the cross-product result by Eq. (25).

Then the camera is commanded to point to the target side with this approximate roll angle; its boresight shadow on the LH plane is further used to the second round of refinement, with the same algorithms as in Sec. II.E, to guarantee that the position and velocity vectors of the camera's boresight projected onto the LH plane are exactly perpendicular. With the refined results Eq. (37) is used once more to determine the final roll angle of the camera's boresight axis. The required roll angle of the satellite is then obtained by taking into account the initial canted angle of the camera, with the following formula:

$$\Phi = \Phi_B - \tau \tag{37}$$

V. Prediction of Imaging Projection at Given Time and Attitudes

In many applications it is required to predict the exact imaging projection point onto the Earth's surface for a specified time and known orientation of the satellite. In other words, the camera's orientation with respect to the orbital axes are given, then the camera's boresight's projection location on the Earth's surface at a specified time needs to be determined. This is a much simpler task compared to that in the preceding three working modes, discussed in Secs. II–IV.

The computation is performed in the ECEF axes, based on the satellite position vector and the camera's boresight direction vector. With the epicycle orbital propagation model described by Eqs. (17–21), the satellite position in the inertial space at the specified time can be easily determined and then transformed into the ECEF axes. On the other hand, the unit orientation vector of the camera's boresight can be easily determined in the LO axes based on the given orientation angles. Assuming the camera is mounted in the satellite nadir direction, the satellite orientation is given as three attitude angles, i.e., the roll angle Φ, pitch angle Θ, and yaw angle Ψ. Based on the transformation matrix A_{321} between body and orbital reference frames,[13] the camera's orientation vector in the LO axes can be determined as

$$\boldsymbol{c}_{\text{LO}} = \begin{bmatrix} -\cos\Phi\cos\Theta \\ \sin\Phi\sin\Psi + \cos\Phi\cos\Psi\sin\Theta \\ \sin\Phi\cos\Psi - \cos\Phi\sin\Psi\sin\Theta \end{bmatrix} \tag{38}$$

This vector is further transformed into ECI and ECEF frames successively. In ECEF the position vector of the imaging point on the Earth's surface should have the following relation:

$$\boldsymbol{p}_{\text{ECEF}} = \boldsymbol{r}_{\text{ECEF}} + d \cdot \boldsymbol{c}_{\text{ECEF}} = \begin{bmatrix} x_p \\ y_p \\ z_p \end{bmatrix} \tag{39}$$

where $\boldsymbol{p}_{\text{ECEF}}$ is the position vector of the image point to be determined and d is the length of the slant vector from the satellite to the image point. Now the task becomes to determine the distance d from the satellite to the Earth's surface along the camera's boresight orientation.

As the imaging projection point lies on the Earth's surface, the following constraint on its position vectors exists:

$$\left[\left(x_p^2 + y_p^2\right)/a^2\right] + z_p^2/c^2 = 1 \tag{40}$$

where a, c are the Earth's equatorial and polar radii. This relation results in a quadratic equation in d, which could be easily solved. Then the resulted $\boldsymbol{p}_{\text{ECEF}}$ is the imaging projection point on the Earth's surface.

VI. Software Development and Test Computations

Stimulated by the practical demands for Tsinghua-1 imaging missions, the preceding algorithms and a software package have been developed in Surrey Space Center. The software was developed with standard C in Unix environment. It comprises the four working modes discussed in this paper and the basic working mode to predict rise-and-set times and maximum elevation angle time[7] as well. The software will read the NORAD orbital data file, which is freely available for all traded satellites over the Internet,[10] and translate it into epicycle elements.[9] Then based on the assigned target information and working mode choices, all of the potential imaging chances will be predicted, and appropriate results will be

Table 4 Imaging prediction results at two working modes

Parameter	Nadir imaging (canted at 0 deg)			Canted at −20 deg	
Imaging time	03:06:49.67 06/09/2000	13:44:14.08 10/09/2000	03:14:58.22 11/09/2000	02:50:30.62 08/09/2000	14:00:32.03 08/09/2000
Elevation angle, deg	83.6675	82.2879	83.4948	60.4456	73.0922

Table 5 Maximum elevation results corresponding to Table 4

Parameter	Nadir imaging (canted at 0 deg)			Canted at −20 deg	
MaxEL time	03:06:49.38 06/09/2000	13:44:14.37 10/09/2000	03:14:57.94 11/09/2000	02:50:31.84 08/09/2000	14:00:30.74 08/09/2000
Elevation angle, deg	83.6701	82.2900	83.4973	60.4529	73.1072
Time err, s	−0.29	0.29	0.28	1.22	−1.29

stored into data files. This software has now been incorporated into the Tsinghua-1 mission planning and management system in Surrey Satellite Technology Limited (SSTL) for engineering applications. Computation results for both Tsinghua-1 and UoSAT-12 showed that all of the algorithms developed in this paper have good estimation accuracy and fast convergence. After the coarse search and estimation algorithms (steps 1 and 2) the estimated imaging times are within a few seconds (1–3 s) of the actual times. With the developed iteration algorithm (step 3) the time accuracy could reach to 0.02 s within 2–3 rounds of iteration.

Illustrated hereafter is some test computation results with this software. The NORAD orbital data file of Tsinghua-1 on 6 September 2000 (Epoch time: 11:42:58.31 on 05/09/00) is set as the orbital input; the searching time window is set as seven days. The camera's FOV is set as 15 deg. The ground target is chosen as Guildford, United Kingdom (latitude 51.2 deg, longitude 359.41 deg, height 0 m). In the computation of the velocity vectors in the LH plane, a time step of 0.1 s is applied. The error tolerance for estimation refinement is set as 0.02 s. The resulting opportunities found for different working modes are listed here: visible passes, 52; nadir imaging, 3; canted at −20 deg, 2; canted at −20 deg with yaw, 12(7 pass); with roll $\Phi_{max} = 20$ deg, 5; and with roll $\Phi_{max} = 27.5$ deg, 7. Table 4 lists some detailed prediction results at two working modes.

From Table 4 for a time span of one week, there were 52 visible passes over the target; however, only three passes give chances of imaging with a nadir tracking camera. When the camera is canted with −20 deg, only two passes give imaging opportunities. By using yawing control, the imaging opportunities are increased to 12 from seven passes. Similarly, with a maximum roll maneuver of 27.5, all of the seven passes give seven imaging chances. When the maximum roll angle is reduced to 20, the imaging chances are reduced to 5, i.e., five passes are within the canted angle of 20 deg, which contribute two imaging chances in the mode with yaw control.

To evaluate the difference between the imaging time and the maximum elevation time, Tables 4 and 5 give the corresponding prediction results for imaging and maximum elevation angles. As seen, for the nadir tracking the time error is around 0.28 s. When the camera has a cant angle of −20 deg, the differences are increased up to around 1.2 s, which makes significant errors when taking high-resolution images. This result reveals the necessity of developing specific algorithms for imaging predictions.

The prediction accuracy in space is evaluated by checking the miss distance between the target and the camera's boresight shadow point in the LH plane at the predicted time, using the algorithms presented in Sec. V. That is, with the predicted time and attitude information the imaging projection point on the Earth's surface is calculated and compared to the specified target position. Results showed that with yaw maneuvers the miss distances are within 0.1 m for the cases when the camera is able to point at the target. With roll maneuvers the miss distances are within 20 m. This estimation accuracy is good enough for Earth observation missions.

To evaluate the efficiency in computational burden, a comparison test has been done between the new software and the old software used by SSTL, which was developed based on the trajectory checking approach by using the SGP4 propagation model[10] with a constant time step. Both algorithms are run on the same PC with a Pentium III processor of 500 MHz to predict imaging opportunities for 433 targets around the world in a time span of seven days with the orbital data of Tsinghua-1. The time step for the old software was set at 1 s, which means the timing accuracy of the prediction results is within 1 s. The time tolerance for the new software was set as 0.02 s. Results show that for the same working mode (nadir imaging) the new software is approximately 1000 times faster than the old software (0.6 vs 590 s). For the more complicated working modes with attitude controls, the old software cannot provide estimates for comparison. Compared to itself, the computation time is approximately 30–50% larger than that for the nadir imaging mode. Additionally, to achieve the same timing accuracy, the time step for the old software should be reduced to 0.02 s, which means its computation time would increase roughly 50 times. This comparison test indicates the significant improvements of the new algorithms in both accuracy and speed.

VII. Conclusions

This paper presents fast prediction algorithms for predicting the best imaging opportunities for several working modes, including a canted camera and available yaw and roll attitude maneuvers. The prediction is divided into three steps: coarse search, imaging estimation, and imaging refinement. In the first two steps a circular satellite orbit and a spherical Earth are assumed to simplify the computation. The computational errors induced are compensated in the final step, where the exact Earth's shape and accurate orbital propagation model are used to refine the prediction results.

As the secular perturbations, short and long periodic perturbations, and drag influences are taken into account, the developed prediction algorithms are suitable for long-term imaging predictions for the LEO satellite Earth observing missions, with their orbit eccentricity being not larger than 0.005. The software has already been applied by SSTL in the ground-based mission planning for Tsinghua-1 and UoSAT-12 satellites, which proves to be significantly faster than the previous software, while allowing for arbitrary accuracy in the timing.

The algorithms are also appropriate for onboard real-time applications for the purpose of autonomous in-orbit mission management and control of satellite (on-line application), which is planned in Surrey Space Center for future missions.

In more general, the algorithms are also useful for any satellite pointing guidance and target tracking missions.

Acknowledgments

The authors are grateful to Andy Brewer of Surrey Satellite Technology Limited for his efforts to put the software into the imaging mission management system and to run some comparison tests. The helpful comments and suggestions from the reviewers, especially concerning the algorithm improvement in Sec. V, are greatly appreciated.

References

[1]Chu, V., Da Silva Curiel, R. A., Sun, W., and Sweeting, M., "Disaster Monitering Constellation," International Academy of Astronautics, Paper 00-IAA.11.4.03, Oct. 2000.

[2]Da Silva Curiel, R. A., Sun, W., Sweeting, M., Jolly, G., and Stephens, P., "The 'GANDER' Mission," International Academy of Astronautics, Paper 00-IAA.11.4.05, Oct. 2000.

[3]Palmer, P. L., and Mai, Y., "A Fast Prediction Algorithm of Satellite Passes," 14th Annual AIAA/USU Conf. on Small Satellite, Paper SSCOO-VI-5, Logan, Utah, Aug. 2000.

[4]Escobal, Pedro, R., *Methods of Orbit Determination*, Wiley, New York, 1976, pp. 150–186.

[5]Lawton, J. A., "Numerical Method for Rapidly Determining Satellite-Satellite and Satellite-Ground Station in-View Periods," *Journal of Guidance, Navigation, and Control*, Vol. 10, No. 1, 1987, pp. 32–36.

[6]Alfano, Salvatore, and Negron, David Jr., "Rapid Determination of Satellite Visibility Periods," *Journal of Astronautical Sciences*, Vol. 40, No. 2, 1992, pp. 281–296.

[7]Mai, Y., and Palmer, P. L., "Fast Algorithms for Prediction of Satellite Imaging and Communication Opportunities," *Journal of Guidance, Control, and Dynamics*, Vol. 24, No. 6, 2001, pp. 1118–1124.

[8]Vallado, D. A., *Fundamentals of Astrodynamics and Applications*, 2nd ed., Kluwer, New York, 2001, pp. 825–837.

[9]Wertz, J. R. (ed.), *Spacecraft Attitude Determination and Control*, D. Reidel, Dordrecht, The Netherlands, 1985, pp. 727–734.

[10]Hoots, F. R., and Roehrich, R. L., "Models for Propagation of NORAD Element Sets," Office of Astrodynamics, Aerospace Defence Center, Spacecraft Rept. 3, Peterson AFB, CO, Dec. 1988.

[11]Hashida, Y., and Palmer, P. L., "Epicyclic Motion of Satellites About an Oblate Earth," *Journal of Guidance, Control, and Dynamics*, Vol. 24, No. 3, 2001, pp. 586–596.

[12]Mai, Y., and Phil, P. L., "On the Conversion of NORAD Elements to Epicycle Elements," *Journal of Guidance, Control, and Dynamics*, Vol. 24, No. 2, 2001, pp. 406, 407.

[13]Sidi, M. J., *Spacecraft Dynamics and Control*, Cambridge Univ. Press, Cambridge, England, U.K., 1997, p. 102.